Chemical Science

ROYAL SOCIETY OF CHEMISTRY

EDGE ARTICLE

View Article Online
View Journal

Cite this: DOI: 10.1039/d6sc03527b

All publication charges for this article have been paid for by the Royal Society of Chemistry

Enhanced electronic coupling in tetraaryl molecular junctions with osmium(IV) centers

Luana Zagami,[a] Mukund Sharma,[a] Andrew Fraire,[a] Cynthia Avedian,[a] Clarissa Olivar,[a] Thomas M. Czyszczon-Burton,[a] Jazmine Prana,[a] Sandugash Yergeshbayeva,[a] María Camarasa-Gómez,[b] Daniel Hernangómez-Pérez *[c] and Michael S. Inkpen *[a]

Structural motifs based on tetraphenylmethane are widely used in molecular electronic circuits, self-assembled monolayers, and porous frameworks, but their performance in conductive systems is often limited by redox-inactive, sp^3-hybridized central atoms that interrupt π-conjugation. Here, we show that replacing the group 14 central atom with a tetravalent transition metal provides a design strategy to enhance electronic coupling and enable bias-dependent control of charge transport. We demonstrate this by measuring the single-molecule conductance of oligoaryl wires incorporating tetrahedral osmium(IV), silicon, or carbon centres using scanning tunnelling microscope-based break junction measurements. In non-polar solvents, junctions comprising osmium(IV) complexes exhibit a significantly reduced conductance decay with length compared to their organic analogues. In polar media, their conductance can be electrochemically modulated to values up to 80× higher than those of a silane analogue. Combined electrochemical and spectroscopic studies, supported by first-principles calculations, indicate that osmium(IV) wires exhibit more delocalized frontier orbitals and smaller HOMO–LUMO gaps, leading to well-coupled HOMO-derived transmission resonances near the electrode Fermi level. Together, these results establish transition metal tetraaryl complexes as promising building blocks for molecular circuits and extended materials.

Received 27th April 2026
Accepted 10th June 2026

DOI: 10.1039/d6sc03527b

rsc.li/chemical-science

Introduction

In the development of molecular components that can function as electronic circuit elements such as wires or switches, most work has focused on one-dimensional (1D) species functionalized with two linker groups to establish connections to nanoscale electrodes.[1] This focus reflects the substantial challenges[2] in moving beyond studies of *two-terminal* junctions formed using scanning probe,[3–5] or eutectic gallium-indium[6] methods. Nonetheless, several studies have begun to explore the properties of multi-terminal,[2,7,8] or branched,[9–13] molecular junctions. Looking ahead, it may prove possible to assemble extended molecular circuits by connecting individual components through bridging molecule-based nodes. Such nodes could electronically couple circuit elements, isolate them to preserve their independent function, or serve both roles through reversible switching. Progress towards this goal requires systematic evaluation of molecular architectures that control transport through well-defined two- or three-dimensional (2D or 3D) geometries. These architectures may also be relevant to conductive, permanently porous materials such as covalent organic frameworks (COFs)[14] and metal–organic frameworks (MOFs).[15] In these systems, electronic coupling between molecular sub-units governs band dispersion and, consequently, charge carrier mobility and conductivity.[15,16] Single-molecule conductance measurements provide a complementary approach to probe trends in such electronic interactions, for example through conductance-distance relationships,[1] and may offer insight into how node structure influences long-range transport behaviour.[17–21]

Tetratopic building blocks based on tetraphenylmethane or silane cores represent a prototypical class of 3D molecular nodes. These redox-inactive motifs, which feature a sp^3-hybridized central atom, have been widely employed in self-assembled monolayers, molecular junctions,[22–34] and porous polymeric materials.[35–38] However, the interruption of π-conjugation between aryl arms results in relatively weak electronic coupling across these nodes, which can limit their application in conductive systems. Efforts to address this limitation have included the development of partially conjugated tetratopic analogues for single-molecule junction studies.[39–43] Interestingly, electrically conductive 3D COFs and MOFs remain

[a]Department of Chemistry, University of Southern California, Los Angeles, CA 90089, USA

[b]Centro de Física de Materiales (CFM-MPC) CSIC-UPV/EHU, 20018 Donostia-San Sebastián, Spain. E-mail: inkpen@usc.edu

[c]CIC NanoGUNE BRTA, Tolosa Hiribidea, 76, 20018 Donostia-San Sebastián, Spain. E-mail: d.hernangomez@nanogune.eu

comparatively rare[39,44,45] relative to their 2D counterparts,[15] and often employ distinct 3D node structures. Furthermore, these extended materials frequently incorporate redox-active components, which are thought to facilitate charge transport through hopping mechanisms and/or by increasing charge carrier density upon partial oxidation or reduction (doping).[15]

We hypothesized that replacement of the sp^3-hybridized atom in a tetraphenyl node with a tetravalent transition metal[46] could provide a strategy to enhance electronic coupling between π-conjugated aryl substituents. The success of this approach was not *a priori* certain: while transition metal complexes have long been explored in molecular junctions and can in some cases exhibit enhanced conductance relative to organic analogues,[47–49] previous studies have also shown that conductance and junction stability can vary substantially depending on the metal centre and ligand framework.[50,51] Nonetheless, osmium(IV) tetraaryl complexes represent an attractive platform due to their established air, thermal, and solution stability, well-developed synthetic chemistry, and accessible, reversible redox behaviour.[52–58] Their frontier orbitals are expected to exhibit metal–ligand d-π character, facilitating orbital delocalization across the central atom.[59] Indeed, recent spectroelectrochemical studies of ferrocenyl-appended osmium(IV) tetraaryl complexes revealed signatures of electronic communication between peripheral redox centres.[53] However, the extent of coupling across different central atoms could not be assessed, as mixed-valence states of silane and methane analogues proved difficult to access. This limitation motivated us to study an analogous series of linker-functionalized compounds, enabling direct, isostructural comparison of the influence of central atom identity on charge transport. More broadly, this approach extends previous investigations into how substitution of $-CH_2-$ units in molecular wire backbones with main group fragments based on nitrogen,[60,61] oxygen,[17] silicon,[60,62] or germanium[63] influences junction conductance.

Accordingly, we synthesized and studied three families of molecules comprising tetravalent osmium (**Os-*n***), silicon (**Si-*n***), and carbon (**C-*n***) centres tetrahedrally coordinated by four identical linker arms (Fig. 1a,b). Each arm consists of a conjugated oligomeric wire with $n = 1$–3 *para*-substituted aryl units, terminated with a thioether group for electrode binding. The *pseudo*-tetrahedral symmetry of these compounds, together with the rapid rotation of phenyl rings at room temperature, renders each linker arm effectively equivalent on the timescale of our conductance measurements. As such, we describe these compounds as "*isotropic*" or orientation-independent conductors, in the sense that equivalent transport pathways are probed for different linker combinations within a given junction geometry. For example, when any one thioether binds to each electrode (the "1 : 1 configuration"), transport occurs through the same −oligoaryl−M−oligoaryl− motif (Fig. 1c, *left*; M = Os, Si, C). This contrasts with other tetratopic nodes, such as 1,3,6,8-substituted pyrenes, where distinct transport pathways are accessed depending on which linker groups are connected (Fig. 1c, *right*).

Single-molecule conductance measurements reveal two dominant conductance features for each molecular wire studied. The lower conductance feature is consistent with

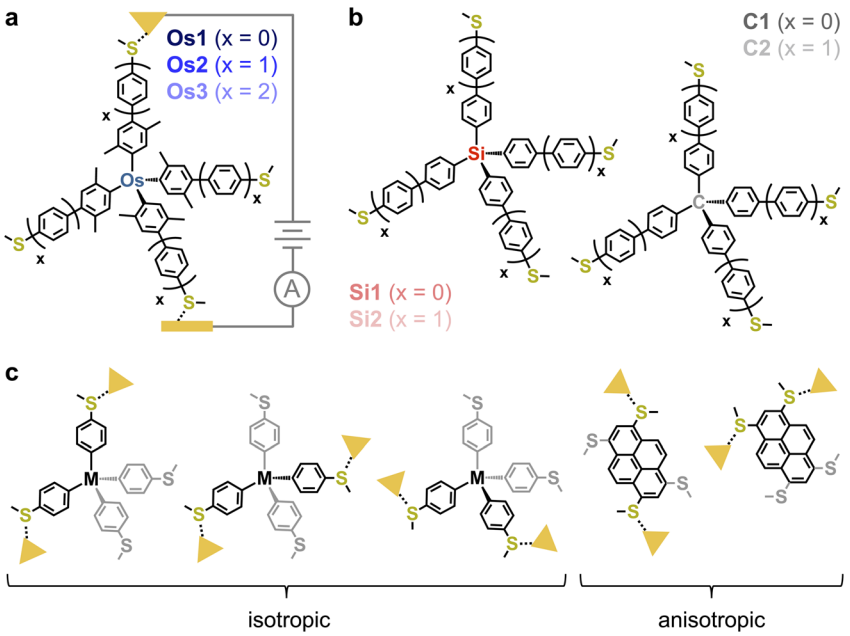

Fig. 1 (a) Schematic of a single-molecule junction comprising model tetraarylosmium(IV) complexes with mono, bi, or triaryl linker arms terminated with thioether groups (**Os-*n***). Here **Os-*n*** is shown connected to each electrode *via* a single thioether group (a "1 : 1 configuration"). (b) Chemical structures of tetraarylsilane and tetraarylmethane analogues. (c) *Left:* We describe these tetraaryl wires as "*isotropic*" or orientation-independent conductors, meaning that equivalent through-bond transport pathways are probed for different thioether-electrode contacts (three of six possible examples illustrated; M = Os, Si, C). *Right:* In contrast, other tetratopic components such as 1,3,6,8-substituted pyrenes can be described as *anisotropic* conductors, exhibiting distinct through-bond transport pathways depending on which thioether groups are connected (two examples illustrated).

junctions comprising intact molecular species bound to both electrodes by thioether linker groups, whereas the geometry corresponding to the higher conductance feature cannot yet be unambiguously assigned. In tetradecane (TD, a non-polar solvent), terminally anchored **Os-*n*** junctions exhibit a smaller tunnelling decay with increasing linker arm length compared to their **Si-*n*** and **C-*n*** analogues, such that the conductance of the longer wires is higher by at least a factor of 3–5. In propylene carbonate (a polar solvent), the conductance of terminally anchored **Os2** junctions can be electrochemically modulated to values >80× higher than those of **Si2** measured under the same conditions. These findings are supported by solution electrochemistry, UV-vis spectroscopy, molecular orbital considerations, and gas-phase density functional theory (DFT), which indicate that **Os-*n*** compounds exhibit frontier orbitals with greater delocalization and smaller HOMO–LUMO gaps than their **Si-*n*** and **C-*n*** counterparts. DFT-based quantum transport calculations further support the experimental trends, showing that transmission resonances derived from the delocalized HOMOs of **Os-*n*** are well-coupled to the electrodes and lie close to the Fermi level (E_F). Together, this work introduces transition metal σ-aryl complexes as a distinct class of organometallic wires that exhibit enhanced conductance relative to isostructural organic analogues. It further demonstrates that the intact compounds can be studied reproducibly under break-junction conditions, in contrast to some other metal-containing species.[51] Looking ahead, our study also motivates future efforts to explore the unique properties of single-molecule junctions and extended materials built from these and related metal-containing systems.

Results and discussion

Synthesis and structural characterization

The monoaryl compounds **Os1** and **Si1** were synthesized through direct reaction between aryl magnesium bromide or aryl lithium with $(Oct_4N)_2[OsBr_6]$[52,54] or $SiCl_4$,[64] respectively, whereas **C1** was prepared through nucleophilic substitution of tetrakis(4-bromophenyl)methane with sodium thiomethoxide (Fig. 2a).[65] The oligoaryl compounds were prepared through Suzuki cross-coupling[57] of 4-(methylthio)phenylboronic acid or 4-(4-methylthiophenyl)phenylboronic acid with tetrakis(4-bromo-2,5-dimethylphenyl)osmium(IV),[53] tetrakis(4-bromophenyl)silane, or tetrakis(4-bromophenyl)methane. All compounds were isolated as solids that readily dissolved in common organic solvents and proved air-stable even in solution. Unoptimized yields ranged between 9–34% (55–76% per bond). The structure of **Si1** was further verified through single-crystal X-ray diffraction (Fig. S1). As **Si3** and **C3** (analogues of **Os3** with Si/C central atoms) were projected to exhibit a conductance below the noise floor of our instrument, their synthesis was not pursued. While $Os(aryl)_4$ complexes are known to react with small Lewis acids such as PMe_3, isocyanides, or CO,[56] we find they do not react with the thioethers introduced here, likely due to the steric bulk of the associated aryl group.

The electronic properties of **Os-*n*** were probed in solution electrochemical and spectroscopic studies, given that $Os(aryl)_4$ complexes are known to exhibit reversible redox chemistry and strongly absorb in the visible region.[53–55,66,67] Data for all compounds are provided in Tables S2 and S3. In Fig. 2b, we plot overlaid cyclic voltammograms for **Os-*n*** in $^nBu_4NPF_6$–CH_2Cl_2. These measurements reveal reversible redox features corresponding to 0/1+ and 1−/0 events ($i_{pa}/i_{pc} \sim 1$, $i_p \propto \nu_s^{1/2}$) which have previously been assigned to the $Os^{4+/5+}$ and $Os^{3+/4+}$ couples, respectively.[55] **Os1** also exhibits a 1+/2+ redox feature that has been observed for some other complexes bearing para-substituted aryl ligands.[52,54]

Notably, the electrochemical gap of these materials (1.97–2.15 V) increases from **Os1** to **Os2** ∼ **Os3** (with increasing linker arm length). This trend contrasts with that expected for conjugated organic materials, where HOMO–LUMO gaps decrease with increasing conjugation length. In **Os-*n***, the frontier orbitals have significant metal–ligand d-π character, such that

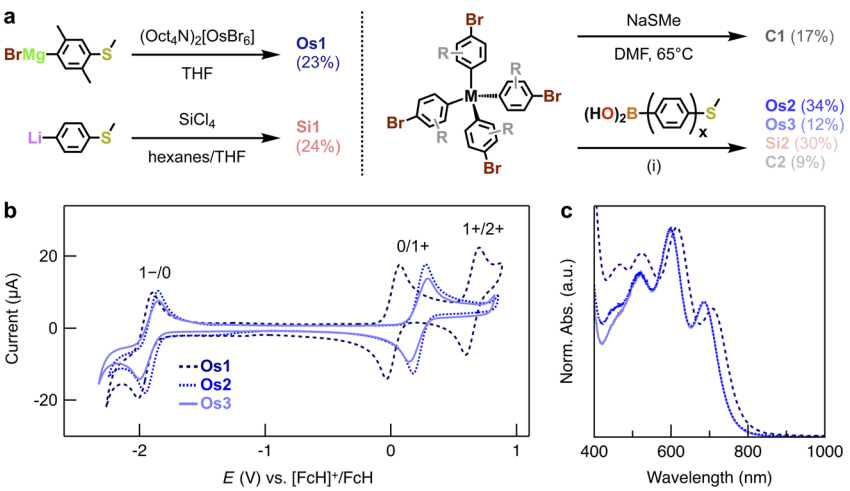

Fig. 2 (a) Synthetic routes to tetraaryl compounds ($x = 1$, **Os2**, **Si2**, **C2**; $x = 2$, **Os3**). *Conditions:* (i) $Pd(PPh_3)_4$, K_2CO_3, DMF, 110 °C. (b) Overlaid cyclic voltammograms of **Os-*n*** (potentials are reported relative to the ferrocenium/ferrocene, $[FcH]^+$/FcH, redox couple). (c) Overlaid UV-vis spectra for **Os-*n***, normalized to the maximum absorption in the visible region (additional spectra are provided in Fig. S2).

their energies respond differently to extension of the ligand backbone. For example, the relatively small HOMO–LUMO gap of **Os1** has been attributed to a high-lying HOMO with metal–ligand character, destabilized relative to the LUMO by resonance contributions from proximal thioether substituents.[52] As the ligand backbone is extended, the HOMO is stabilized relative to the LUMO (*i.e.*, lowered in energy), leading to an increase in the HOMO–LUMO gap (Table S10).

In Fig. 2c, we plot overlaid UV-vis spectra for **Os-*n*** measured in CH_2Cl_2, which show four strong absorption bands in the visible region characteristic of this family of complexes.[52,66,68] The trends in optical gaps (785–757 nm, 1.58–1.64 eV) correlate with those of the electrochemical gaps, indicating that these energy level spacings are intrinsic properties of the complexes. In contrast to the trends observed for **Os-n**, **Si-*n*** and **C-*n*** ($n = 1$–2) exhibit much larger optical gaps (≤335 nm, >3.7 eV) that decrease with increasing linker arm length, as expected for π-conjugated systems (Fig. S2).

The qualitative differences in electrochemical and optical gaps between the organic wires and **Os-*n*** may be rationalized based on their electronic structure. In the organic systems the sp^3-hybridized central atom restricts π-conjugation to individual linker arms, resulting in relatively large gaps. In **Os-*n***, which adopt tetrahedral geometries, the HOMO and LUMO are derived from orbitals of mixed metal and ligand character, corresponding to the orbital sets with e and t_2 symmetry, respectively. This is consistent with the DFT-calculated frontier orbital compositions (Fig. S19). The HOMO–LUMO gap therefore reflects the tetrahedral splitting energy (Δ_{tet}). While the strong ligand field provided by the four σ-aryls in **Os-*n*** is sufficient to provide a Δ_{tet} that is greater than the electron pairing energy, as evidenced by the d^4 low-spin (diamagnetic) character of these complexes, Δ_{tet} is generally smaller than splitting energies for other common coordination geometries.[59] For example, with all else equal, $\Delta_{tet} = 4/9\Delta_{oct}$,[69] where Δ_{oct} is the octahedral splitting energy.

Conductance measurements in non-polar solvents

We next perform single-molecule conductance measurements using the STM-based break junction (STM-BJ) method with custom-built instrumentation which has been described previously (see Methods).[21,70] In Fig. 3a–c, we present overlaid 1D conductance histograms for **Os-*n***, **Si-*n***, and **C1** measured in TD, as well as **C2** measured in 1,2,4-trichlorobenzene (TCB). Under these conditions, histograms show two conductance peaks that are reproducible within a factor of ∼2 (Fig. S3 and S8b). We associate both high and low conductance features with junctions formed from the parent compounds, as the conductance of these peaks systematically decreases with increasing number of aryl groups in each linker arm (Fig. 3e and f). We note that histograms for **C2** measured in TD do not show a clearly resolved low conductance peak, which we attribute to this feature being too low in conductance and/or sloped to resolve above the instrumental noise floor. Accordingly, data obtained in TCB likely provides an upper bound for the conductance of **C2** junctions under these conditions. In Fig. 3d, we present an illustrative 2D histogram for **Os2**, showing that the step features corresponding to both high and low conductance junction extend to ∼0.5 and ∼1 nm, respectively. Corresponding 2D histograms for other **Os-*n***, **Si-*n***, and **C-*n*** compounds are provided in Fig. S4 and S8d, which show that step lengths for both conductance features are similar for compounds with linker arms comprising the same number of aryl groups, even when connected to different central atoms. For completeness, we note that the low conductance feature observed for **Os1** junctions is best resolved at lower V_{bias} (Fig. S3), but data are presented here at $V_{bias} = 750$ mV for all compounds for consistency, and to ensure histogram features are resolved above the instrument noise floor. Conductance peaks for **Os-*n***, **Si-*n***, and **C-*n*** do not otherwise exhibit a strong bias-dependence in TD.

Focusing first on the lower conductance features, we note that their maximum displacement is close to the calculated S–S distance for each compound obtained from DFT-optimized structures after accounting for the gold snapback distance of ∼0.6 nm.[71,72] For **Os1**, **Si1**, and **C1**, the step displacement is ∼0.4 nm, compared to calculated S–S distances of ∼1.1 nm (Fig. S4). For **Os2** and **Si2** the step displacement is ∼1 nm, with calculated S–S distances of 1.7–1.9 nm (Fig. 3d and S4d). These observations are consistent with junctions formed by intact molecules bridging the electrodes *via* terminal linker groups (*i.e.*, a 1 : 1 configuration; Fig. 1a). To further support this junction geometry assignment, we synthesized and studied a control molecule, **Si2 (−2PhSMe)**, containing only two linker groups and therefore restricted to binding in a 1 : 1 configuration (Fig. S6). The step length, shape, and conductance of **Si2 (−2PhSMe)** junctions closely match those observed for **Si2** (2.9×10^{-7} *vs.* 3.5×10^{-7} G_0, respectively). This assignment is qualitatively consistent with the comparable conductance of **Si1** junctions to those formed from a structurally related two-linker system reported in the literature, albeit measured using a different bias and solvent.[62] As indicated by transmission calculations for junctions comprising **Si2 (−2PhSMe)** and related compounds, discussed further below, small conductance differences between these compounds may be attributed to modifications of the other substituents on the central silicon atom (Fig. S26). While we cannot exclude conductance contributions from junction configurations involving the binding of multiple linker groups of **Os-*n***, **Si-*n***, and **C-*n*** compounds to a single electrode (*e.g.*, 1 : 2 or 2 : 2), such configurations are expected to be less probable due to the large separation between sulfur atoms (∼1–2.6 nm) and the localized nature of under-coordinated gold binding sites formed upon junction rupture. Such configurations may exhibit similar conductance values or contribute to features at shorter displacements, in line with the observed histogram features.

In Fig. 3e, a plot of peak conductance against n for these features reveals that the conductance of **Os1**, **Si1**, and **C1** junctions is comparable. In contrast, **Os2** junctions formed in TD exhibit a higher conductance than those of **Si2** in TD/TCB and **C2** in TCB by factors of approximately 3 to 5, a trend that holds across repeated measurements (Table S4). While the low conductance feature of **Os3** is not well resolved above our

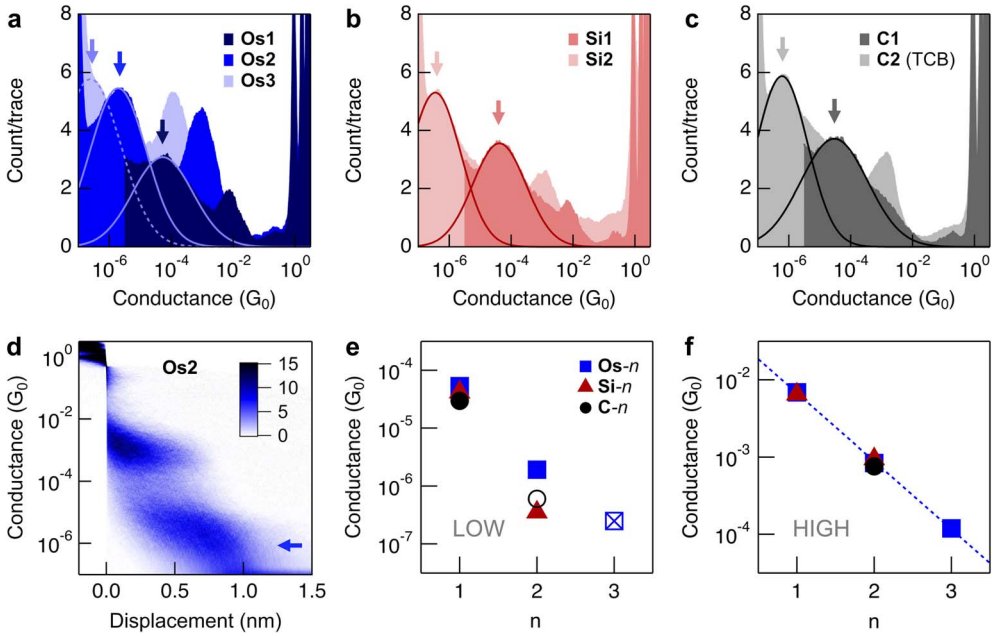

Fig. 3 Overlaid 1D histograms for (a) **Os-*n***, (b) **Si-*n***, and (c) **C-*n*** (≥5000 traces). All measurements were performed with $V_{bias} = 750$ mV in TD, except for **C2** which was measured in TCB. Arrows indicate the low conductance features assigned to junctions formed by intact molecules bridging the electrodes *via* thioether linker groups (*e.g.*, a 1 : 1 configuration, Fig. 1a). These features are fit with Gaussian functions to obtain the most probable conductance values. (d) 2D conductance histogram for **Os2**; additional 2D histograms are provided in Fig. S4 and S8d. (e) Plot of peak conductance *versus n* for the low conductance features in panels (a–c) (TD = solid symbols, TCB = hollow symbols). The datapoint for **Os3** (checked square) is approximate, as the associated conductance feature is not well resolved above the instrument noise floor (dashed line fit in panel (a)). (f) Plot of peak conductance *versus n* for the high conductance features. A fit to $G = G_c \times \exp(-\beta n)$ for **Os-*n*** gives $\beta = 2.0$ per aryl unit (dashed line). Data for **C1** (no clear high conductance feature observed), and for **Si3** and **C3** (not measured) are excluded. Conductance data for all compounds is provided in Table S4.

instrument noise floor, the most probable conductance of these junctions can be approximated (dashed fit in Fig. 3a). Taken together, these data indicate that the decay of conductance with increasing linker arm length is shallower for **Os-*n*** than for **Si-*n*/C-*n***. These results are even more notable given that the steric influence of the methyl substituents in the 2,5-xylyl groups coordinated to osmium might be expected to limit π-conjugation through the oligoaryl ligand arms by increasing aryl–aryl dihedral angles, thereby reducing junction transport.[4] These methyl substituents, which facilitate the synthesis and stability[73] of the **Os-*n*** complexes, are also expected to influence the equilibrium geometry around the central atom (SI, Geometric analysis), and may introduce minor variations in the S(Me)–Au coordination geometries sampled in **Os1** junctions. This is corroborated by geometry optimization studies of $Si(aryl)_4$ models with and without added methyl substituents (Table S6), as well as transmission calculations of analogous **Si2** junctions (Fig. S26), which reveal clear differences. Accordingly, we emphasize that the present study compares compounds featuring Os−2,5-xylyl, Si−phenyl, and C−phenyl central fragments, rather than isolating the influence of the tetrahedral central atom alone. Despite these structural differences, junctions featuring the Os−2,5-xylyl motif can exhibit higher conductance across the series studied.

We next comment on the key characteristics of the higher conductance features, which are observed for all compounds except **C1**. A plot of peak conductance *versus n* for measurements in TD shows that these features are largely independent of the central fragment and decrease exponentially with increasing linker arm length (Fig. 3f; see Fig. S8 for measurements in TCB). A fit to the **Os-*n*** series yields a tunnelling decay constant, β, of 2.0/*n*, consistent with values typically observed for oligoaryl-based molecular wires.[4,74] The maximum displacement of these features is approximately half that of the corresponding low-conductance features, suggesting that these junctions may involve shorter effective transport pathways. However, the junction geometries associated with these higher conductance features cannot be unambiguously assigned based on the available data. Possible contributions may arise from alternative binding geometries or junction configurations distinct from those associated with the low-conductance features. A more detailed evaluation of the high conductance features, including additional experimental data and analysis (*e.g.*, 2D cross-correlation histograms),[75] is provided in the SI (Analysis of high conductance features). Notably, push–pull measurements of **Os2** indicate that its junctions can be mechanically switched between high and low conductance states, corresponding to an on/off ratio of $>10^2$ (Fig. S12). This observation highlights the dynamic nature of junction formation, however, a detailed mechanistic understanding of this switching process is beyond the scope of the present study.

In addition, we note that measurements of terminally anchored **Os-*n*** junctions in TCB exhibit greater variability than those in TD. As illustrated in Fig. S7a,c,e, the lower conductance feature of **Os2** varies by a factor of ~8, reaching values up to $1.4 \times 10^{-5}\ G_0$ (approximately an order of magnitude higher than in TD). In some experiments, it appears that the corresponding feature for **Os3** can be resolved above the instrument noise floor (Fig. S7b,d,f). These observations contrast with measurements of the organic wires in TCB, which yield more reproducible conductance features (Fig. S8). The origin of this variability is not fully established but may reflect changes in conducting orbital-E_F energy level alignment or partial *in situ* oxidation of **Os-*n*** under these conditions. A detailed exploration of solvent effects is not pursued here; however, the use of TCB may complicate measurements of chemically sensitive or redox-active compounds (particularly under applied electric fields at or near the junction). Aromatic chlorinated solvents are known to interact with gold surfaces to a limited extent, influencing level alignment.[76] Related solvents such as $CDCl_3$ or CH_2Cl_2 can be weakly acidic due to the photogeneration of HCl,[77] or participate in charge-transfer processes that may affect redox-active species.[78] Notably, absorption spectra of **Os2** in CH_2Cl_2, TCB, and TD do not show significant differences indicative of protonation or oxidation in solution (Fig. S2c). The greater consistency of **Os-*n*** measurements in TD is therefore consistent with the non-polar, inert character of this solvent, which minimizes interactions with the electrode surface and limits stabilization of charged species.

Tuning the conductance of Os2 in a polar solvent

To further assess the potential for **Os-*n*** junctions to vary in conductance with level alignment, we performed additional measurements of **Os2** in a third solvent, propylene carbonate (PC). In these experiments, a wax-coated tip was used to minimize background faradaic and capacitive currents that would otherwise obscure the tunnelling currents of interest.[79] However, because the exposed tip electrode area (~1 μm) is small relative to that of the substrate (~1 cm^2), a dense double-layer forms at the tip. This is known to induce a bias-dependent shift of the transmission function relative to the average E_F of the junction.[80] As a result, the applied bias window opens asymmetrically about E_F, enabling experiments that probe the transmission landscape of the junction,[80] provide insight into whether the dominant conducting orbital is occupied or unoccupied,[80,81] and, in some cases, give rise to significant current rectification.[82]

In Fig. 4a and b, we present overlaid 1D histograms for **Os2** measured in PC (no added electrolyte) at different tip biases, across two independent experiments. The conductance of the feature attributed to intact **Os2** junctions increases as the tip bias is made more positive. Gaussian fits to this feature in each histogram indicate that the most probable conductance can be modulated by up to a factor of 47. In Fig. 4c, these results are summarized by plotting the fitted peak conductance values as a function of tip bias, which also demonstrates good reproducibility between experiments at a given bias. Representative 2D histograms in Fig. 4d and e show that the maximum junction displacements associated with the lower conductance features are comparable to those observed in TD measurements (Fig. 3d) and do not significantly vary with tip bias (additional 2D histograms are plotted in Fig. S15). This is consistent with the assignment of this bias-dependent feature to intact molecular junctions. In Fig. 4f, we provide a cyclic voltammogram of **Os2** obtained *in situ* using a gold STM tip as the working ultramicroelectrode and the substrate as both counter and quasi-reference electrode (recorded during the experiment shown in Fig. 4b). A redox wave is observed at ~0.8 V under these conditions, corresponding to approximately +0.65 V *versus* $[FcH]^{0/1+}$ measured under identical conditions (Fig. S16). As this feature is not observed in the absence of **Os2**, it is assigned to the 0/1+ redox event of the complex, shifted by +400 mV relative to measurements in $^nBu_4NPF_6$–CH_2Cl_2 (Fig. 2b). These results indicate the bias window opens towards the HOMO resonance as the tip bias is made more positive. We find that junction formation becomes increasingly difficult for tip biases above +700 mV. This behaviour has also been observed in studies of other molecular junctions at high bias, including systems with transmission resonances close to E_F.[80]

These experiments suggest that terminally anchored **Os2** junctions exhibit a sloped transmission function near E_F, with transport dominated by occupied states,[80] in agreement with the calculations discussed below. Comparison measurements tracking the low conductance feature of **Si2**, as well as the high conductance features of both **Os2** and **Si2**, show much smaller or negligible changes in conductance with tip bias (Fig. 4a–c and S17). This behavior is indicative of transmission functions that are relatively flat around E_F. The high conductance feature of **Os2** also decreases in intensity as the tip bias is made more positive, and appears similarly suppressed at positive biases for **Si2**. Such molecule-specific variations in peak intensity with changing tip bias in PC have been reported previously.[80] Overall, these measurements of **Os2** in PC (Fig. 4a–c) support the view that variations in level alignment can lead to substantial changes in the low conductance feature of **Os-*n*** junctions, comparable in magnitude to those observed across repeated measurements in TCB (Fig. S7), while having a limited effect on transport through **Si2** junctions (Fig. S17). At a tip bias of +700 mV, the conductance of **Os2** junctions is ~83× larger than for **Si2**, highlighting the distinct electronic properties of these structurally analogous compounds.

Computational analyses of model systems in the gas phase

To gain further insight into the electronic properties of these junctions, we now turn to quantum transport calculations. Our calculations are based on density functional theory (DFT) and the non-equilibrium Green's functions formalism, and are performed using the combination of FHI-aims[83] and the transport module AITRANSS.[84–87] Additional computational details can be found in the SI. We show, in Fig. 5a, overlaid transmission functions for **Os-*n*** junctions bound to gold electrodes with two thioether linkers. An example of these relaxed junction geometries is given in Fig. 5c. We observe that the

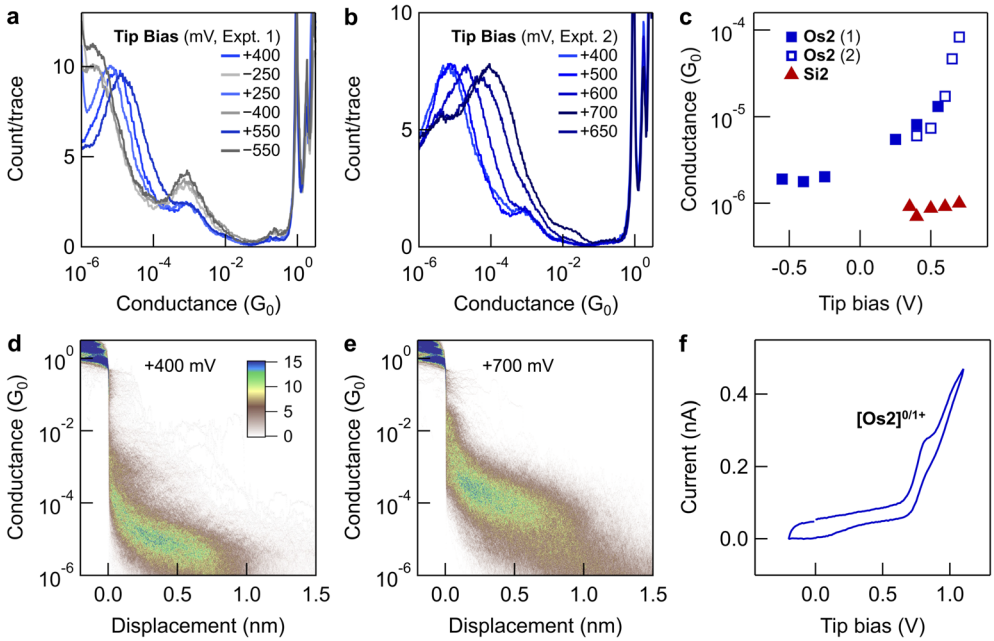

Fig. 4 (a and b) Overlaid 1D histograms (2000 traces) for measurements of **Os2** in PC at different tip biases, acquired in two independent experiments (biases listed in order of measurement). The conductance of the primary feature increases by up to a factor of 47 with changing tip bias. (c) Fitted peak conductance values for **Os2** as a function of tip bias (blue), derived from the data in panels (a) and (b). Corresponding measurements for **Si2** in PC show a substantially weaker dependence on tip bias (red; see Fig. S14 for histograms). (d and e) 2D histograms obtained at tip biases of = +400 mV and +700 mV, respectively, corresponding to the 1D histograms in panel (b). Additional 2D histograms corresponding to data shown in panel (a) are provided in Fig. S12. (f) Cyclic voltammogram obtained using the same tip, substrate, and solution as in the STM-BJ measurements in panel (b), recorded with an external potentiostat. The wax-coated STM tip served as the working ultramicroelectrode, and the substrate as both the counter and quasi-reference electrodes (two-electrode configuration). Additional voltammograms are provided in Fig. S16.

conductance, which is proportional to the transmission at E_F, is highest for the smallest complex and follows the trend: **Os1** > **Os2** > **Os3**. When considering the trend in the HOMO–LUMO gaps (see Table S9 and discussion above), the **Os-*n*** series exhibits the opposite behavior to that of conventional conjugated molecular wires (such as **Si-*n*** and **C-*n***), while still exhibiting the expected decay of conductance with length. Here, the conductance ordering is attributed to the alignment of the HOMO level with E_F, along with its decreasing width as the wire length increases. As is common in calculations using semi-local functionals (here, PBE[88]), the computed conductance of **Os-*n*** junctions is overestimated by more than an order of magnitude compared to experiment, a well-understood artifact arising from the limitations of generalized-gradient approximations to DFT functionals.[89,90] Notably, the calculated conductance for **Os3** is low, consistent with experimental observations that it almost falls below our instrumental noise floor.

We have also performed quantum transport calculations for the **Si-*n*** and **C-*n*** molecular junction series. In Fig. 5b, we show a comparison of the transmission functions for $n = 2$ (**Os2**, **Si2**, **C2**), additional results for the entire **Si-*n*** and **C-*n*** series are available in Fig. S25. An example of one of these relaxed junction geometries is shown in Fig. 5d. We recognize that all these junctions exhibit complex transmission functions with Fano-type interference features, which can be attributed to the existence of non-bonded aryl groups in the complexes. The role of non-bonded side groups not directly involved in the main transmission pathway in generating quantum interference effects is well established.[91,92] In the case of the **Si2** junction, we have checked this effect by removing the two non-bonded aryl arms and substituting them with $-CH_3$ groups (Fig. S26). This modification leads to the disappearance of the Fano-type resonances close to E_F. The calculated conductance of **Si-*n*** and **C-*n*** junctions follows the same trend as for **Os-*n***, with **Si1** > **Si2** > **Si3** and the same ordering for **C-*n***. This trend is consistent with the expected tunnelling behaviour of conductance decay with molecular length of conjugated molecular wires.

Our transport calculations show that **Os2** junctions are HOMO conducting and exhibit a significantly higher conductance than junctions formed from **Si2**/**C2**, though the exact difference may change due to differences in E_F alignment and solvent effects (as noted below). This qualitatively aligns with our experimental studies in PC which show that the conductance of intact **Os2** junctions can vary by a factor up to ~80 relative to their **Si2** analogues. Our calculations for **Si2** also recover the flatness of the transmission function close to E_F as suggested by these conductance measurements. The trend is further supported by the orbital character of the HOMO in **Os-*n*** which shows greater density on the central atom (Os d_{z^2}) compared to the sp^3-like character in **Si-*n*** or **C-*n*** (Fig. S21). This facilitates delocalization of the thioanisole π-system, as well as HOMO level pinning by the metal-derived orbitals, and

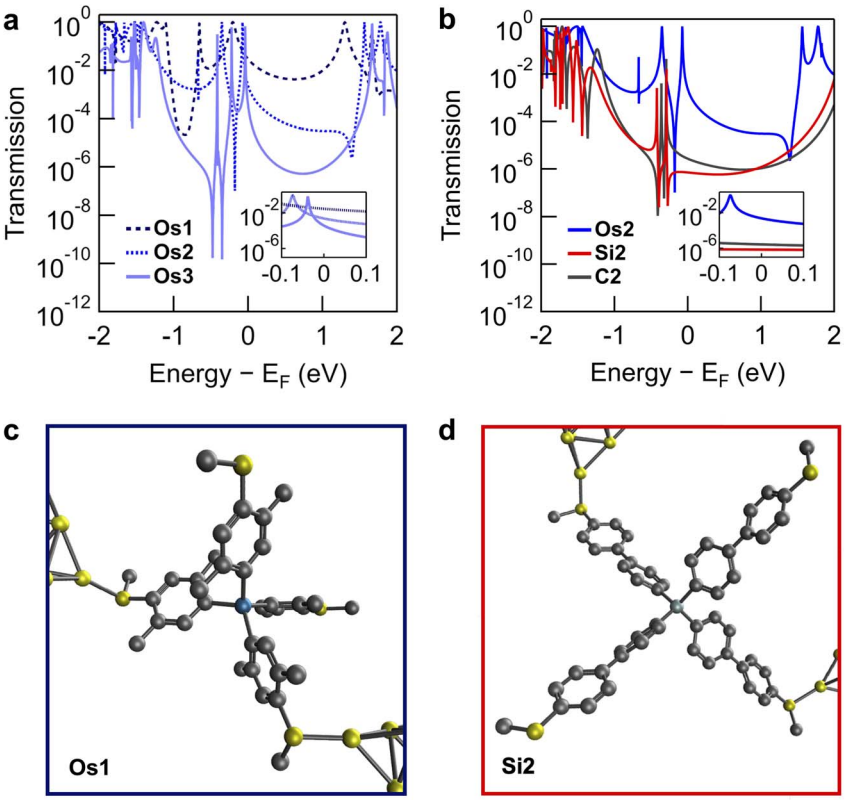

Fig. 5 (a) Overlaid transmission functions for the **Os-*n*** series. (b) Comparison of overlaid transmission functions for **Os2**, **Si2**, and **C2** (data for **Os2** reproduced from panel (a)). Insets provide an expanded view of transmission close to the Fermi level. (c and d) Optimized geometries of **Os1** and **Si2** junctions, respectively. Hydrogen atoms excluded for clarity.

contributes to the higher conductance observed in **Os-*n***. Finally, it is important to stress that our calculations do not account for the effects of solvents or electrochemical influences. This limitation could offer a possible explanation for some discrepancies between the theoretical results and experimental observations.

In closing, we also note that we have calculated PBE-based tunnel couplings, which are related to conductance.[4,93] The results of these calculations align well with the DFT transmission calculations in Fig. 5, consistently recovering highly conductive **Os-*n*** junctions (SI, Tunnel coupling). The tunnel coupling values also indicate that variations in the calculated conductance may result from the orientation of adjacent aryl rings connected through the central atom (explicitly defined, in Fig. S19, using pairs of dihedral angles). While variations due to non-equivalent geometries can also be reproduced in transmission calculations (Fig. S27), these do not change the conductance ordering **Os-*n*** > **Si-*n*** ∼ **C-*n***. To assess the sensitivity of transport predictions and conductance ordering to the choice of exchange-correlation functional, we also performed tunnel coupling calculations using the hybrid functional B3LYP. Tunnel coupling calculations are well suited to hybrid functionals, which should otherwise always be avoided in systems with many gold atoms, as they misrepresent the electronic structure near E_F.[94] We reemphasize that tunnel coupling and full *ab initio* transport calculations show good agreement in capturing the conductance trends, as exemplified by the PBE-based comparison discussed above. Interestingly, the B3LYP-based tunnel coupling calculations suggest that the differences between **Os-*n***, **Si-*n***, and **C-*n*** junctions may be smaller than those predicted by PBE (Tables S7 and S8), in better agreement with experimental trends and providing further insight into the influence of exchange-correlation effects on transport properties.

Conclusion

We have shown, through a combination of experiment and DFT-based calculations, that single-molecule junctions formed from terminally connected osmium(IV) tetraaryl compounds can exhibit substantially higher conductance than analogous organic compounds based on tetrahedral silane or methane cores. Our analysis further suggests that transport through such transition metal complexes can be tuned *via* ligand field modifications, where changes in Δ arising from coordination geometry or ligand field strength directly map onto the HOMO–LUMO gap. The variability observed for **Os-*n*** junctions in TCB and the pronounced, bias-dependent modulation of **Os2** conductance in PC (relative to **Si2**) demonstrate that these organometallic junctions are sensitive to the local (electro)chemical environment, consistent with the sloped character of their calculated transmission functions near E_F. These findings underscore the

importance of controlling the environment around junctions to achieve reproducible conductance measurements for such systems. We propose that **Os-*n*** and related tetraaryl compounds based on other transition metals,[46] as well as structurally distinct σ-aryl complexes (*e.g.*, $OsO(aryl)_4$,[67] $OsO_2(aryl)_2$,[95] or $Os(\eta^6\text{-biaryl})(aryl)_2(L)$[56] where L = PMe_3, CO), may provide a unique modular platform to systematically relate the electronic structure of organometallic components to trends in single-molecule conductance. Beyond single-molecule electronics, these results also support the potential of osmium(IV) tetraaryl complexes as building blocks for 3D ordered polymers with enhanced conductivity, which remains to be evaluated through comparative studies of isostructural bulk materials assembled from different tetrahedral nodes.

Methods

Scanning tunnelling microscope-based break junction

Briefly, we apply a voltage (V_{bias}) between a gold STM tip and gold substrate while pushing these electrodes repeatedly in and out of mechanical contact as we measure the current (I) through the junctions that are produced. Plots of conductance ($G = I/V_{bias}$) *versus* increasing tip-substrate displacement reveal step features at $\sim$1 G_0 (=$2e^2/h$) indicative of the formation of gold–gold atomic point contacts. After breaking the point contacts in the presence of molecules that can bridge the tip-substrate nanogaps, we observe additional conductance step features below 1 G_0 that we attribute to the formation of single-molecule junctions. Thousands of such conductance-displacement traces are compiled without data selection into 1D conductance histograms, whereby the step features combine to provide peaks that can be further fit with Gaussian peaks to obtain the most probable junction conductance. The data is subjected to additional analyses, for example, by constructing 2D histograms that retain the step displacement information. Additional information is provided in the SI.

Computational studies

Tunnel coupling. Density functional theory (DFT) calculations were performed with Q-Chem 5.4.2 and visualized using IQMol 2.15.1.[96] Geometries were optimized at the PBE[88] or B3LYP level (6-31G** for light atoms, LACVP for Os), both with and without single gold atoms bound to sulfur.

Quantum transport calculations. *Ab initio* transport was carried out using FHI-aims[83] with PBE and scalar-relativistic ZORA corrections.[97] Molecular junction geometries were optimized in two steps: relaxation of molecular atoms and apex gold tips (up to 11 atoms per pyramid), followed by addition of gold layers to create the full contacts. Transmission functions were computed *via* linear-response non-equilibrium Green's function formalism using AITRANSS.[84–87] Full computational details can be found in the SI.

Author contributions

L. Z., M. S., A. F., C. A., C. O., S. Y., D. H.-P., and M. S. I. designed and conceived the experiments. L. Z., M. S., A. F., C. A., C. O., T. M. C.-B., J. P., and S. Y. performed experiments. M. C.-G., D. H.-P., and M. S. I. performed calculations. All authors co-wrote the manuscript.

Conflicts of interest

The authors declare no competing financial interest.

Data availability

The data supporting this article have been included as part of the supplementary information (SI). Supplementary information: additional synthetic, spectroscopic, conductance, and computational details and data are available, including synthetic procedures, 1D and 2D conductance histograms, push–pull experiments, 2D correlation analyses, tunnel-coupling and transmission calculations, crystallographic data for **Si1**, and ^1H and $^{13}C\{^1H\}$ NMR spectra for all new compounds. See DOI: https://doi.org/10.1039/d6sc03527b.

CCDC 2480811 contains the supplementary crystallographic data for this paper.[98]

Acknowledgements

This work was primarily supported by funding from the University of Southern California (USC) and the National Science Foundation (NSF CAREER Award to M.S.I., CHE-2239614). D. H.-P. is grateful for funding from the Diputación Foral de Gipuzkoa through Grants 2023-FELL-000002-01, 2024-FELL-000009-01, and 2025-FELL-000004-01. D.H.-P. acknowledges the technical and human support provided by the DIPC Supercomputing Center. M.C.-G. acknowledges support from the Diputación Foral de Gipuzkoa through grants 2024-FELL-000007-01 and 2025-FELL-000009-01, and from grant no. PID2024-159869NA-I00 funded by MICIU/AEI/10.13039/501100011033 and ERDF/EU, and from grant no. PID2022-140845OB-C66 funded by MCIN/AEI/10.13039/501100011033 and ERDF/EU. Instrumentation in the USC Chemistry Instrument Facility was acquired with support from the USC Research and Innovation Instrumentation Award Program. Additionally, funds were provided by the NSF (CHE-2018740) to acquire the X-ray diffractometer used for single-crystal structure determination. Funds provided by the NSF (DBI-0821671, CHE-0840366) and National Institutes of Health (S10 RR25432) supported the acquisition of the NMR spectrometers used in our work.

References

1 T. A. Su, M. Neupane, M. L. Steigerwald, L. Venkataraman and C. Nuckolls, Chemical Principles of Single-Molecule Electronics, *Nat. Rev. Mater.*, 2016, **1**(3), 16002.

2 D. Xiang, H. Jeong, D. Kim, T. Lee, Y. Cheng, Q. Wang and D. Mayer, Three-Terminal Single-Molecule Junctions Formed by Mechanically Controllable Break Junctions with Side Gating, *Nano Lett.*, 2013, **13**(6), 2809–2813.

3 B. Xu and N. J. Tao, Measurement of Single-Molecule Resistance by Repeated Formation of Molecular Junctions, *Science*, 2003, **301**(5637), 1221–1223.
4 L. Venkataraman, J. E. Klare, C. Nuckolls, M. S. Hybertsen and M. L. Steigerwald, Dependence of Single-Molecule Junction Conductance on Molecular Conformation, *Nature*, 2006, **442**(7105), 904–907.
5 D. J. Wold and C. D. Frisbie, Formation of Metal-Molecule-Metal Tunnel Junctions: Microcontacts to Alkanethiol Monolayers with a Conducting AFM Tip, *J. Am. Chem. Soc.*, 2000, **122**, 2970–2971.
6 R. C. Chiechi, E. A. Weiss, M. D. Dickey and G. M. Whitesides, Eutectic Gallium–Indium (EGaIn): A Moldable Liquid Metal for Electrical Characterization of Self-Assembled Monolayers, *Angew. Chem., Int. Ed.*, 2008, **47**(1), 142–144.
7 H. Fu, X. Zhu, P. Li, M. Li, L. Yang, C. Jia and X. Guo, Recent Progress in Single-Molecule Transistors: Their Designs, Mechanisms and Applications, *J. Mater. Chem. C*, 2022, **10**(7), 2375–2389.
8 D. Neuhauser and R. Baer, Phase Coherent Electronics: A Molecular Switch Based on Quantum Interference, *J. Am. Chem. Soc.*, 2002, **124**(16), 4200–4201.
9 A. Błaszczyk, M. Chadim, C. von Hänisch and M. Mayor, Synthesis of Macrocyclic Molecular Rods as Potential Electronic Devices, *Eur. J. Org Chem.*, 2006, **2006**(17), 3809–3825.
10 M. Magoga and C. Joachim, Conductance of Molecular Wires Connected or Bonded in Parallel, *Phys. Rev. B*, 1999, **59**(24), 16011–16021.
11 H. Vazquez, R. Skouta, S. Schneebeli, M. Kamenetska, R. Breslow, L. Venkataraman and M. S. Hybertsen, Probing the Conductance Superposition Law in Single-Molecule Circuits with Parallel Paths, *Nat. Nanotechnol.*, 2012, **7**(10), 663–667.
12 M. S. Inkpen, T. Albrecht and N. J. Long, Branched Redox-Active Complexes for the Study of Novel Charge Transport Processes, *Organometallics*, 2013, **32**(20), 6053.
13 L. E. Wilson, T. T. C. Yue, M. S. Inkpen, I. Grace, A. J. P. White, C. Lambert, T. Albrecht and N. J. Long, Controlling Quantum Interference Patterns in Redox-Active Rings, *J. Organomet. Chem.*, 2024, **1022**, 123368.
14 E. Jin, M. Asada, Q. Xu, S. Dalapati, M. A. Addicoat, M. A. Brady, H. Xu, T. Nakamura, T. Heine, Q. Chen and D. Jiang, Two-Dimensional Sp2 Carbon–Conjugated Covalent Organic Frameworks, *Science*, 2017, **357**(6352), 673–676.
15 L. S. Xie, G. Skorupskii and M. Dincă, Electrically Conductive Metal–Organic Frameworks, *Chem. Rev.*, 2020, **120**(16), 8536–8580.
16 R. Hoffmann, How Chemistry and Physics Meet in the Solid State, *Angew. Chem., Int. Ed.*, 1987, **26**(9), 846–878.
17 H. Li, M. H. Garner, T. A. Su, A. Jensen, M. S. Inkpen, M. L. Steigerwald, L. Venkataraman, G. C. Solomon and C. Nuckolls, Extreme Conductance Suppression in Molecular Siloxanes, *J. Am. Chem. Soc.*, 2017, **139**(30), 10212–10215.
18 A. Jensen, M. Strange, S. Smidstrup, K. Stokbro, G. C. Solomon and M. G. Reuter, Complex Band Structure and Electronic Transmission Eigenchannels, *J. Chem. Phys.*, 2017, **147**, 224104.
19 R. Gutzler and D. F. Perepichka, Π-Electron Conjugation in Two Dimensions, *J. Am. Chem. Soc.*, 2013, **135**(44), 16585–16594.
20 J. K. Tomfohr and O. F. Sankey, Complex Band Structure, Decay Lengths, and Fermi Level Alignment in Simple Molecular Electronic Systems, *Phys. Rev. B*, 2002, **65**(24), 1–12.
21 Z. Miao, T. Quainoo, T. M. Czyszczon-Burton, N. Rotthowe, J. M. Parr, Z. Liu and M. S. Inkpen, Charge Transport across Dynamic Covalent Chemical Bridges, *Nano Lett.*, 2022, **22**(20), 8331–8338.
22 O. A. Al-Owaedi, H. N. Najeeb, A. K. O. Aldulaimi, N. H. Alwan, M. S. Ali, M. H. Dwech and M. A. AL-Da'amy, Thermoelectric Signature of D-Orbitals in Tripod-Based Molecular Junctions, *Mater. Adv.*, 2024, **5**(24), 9781–9791.
23 J. Šebera, M. Lindner, J. Gasior, G. Mészáros, O. Fuhr, M. Mayor, M. Valášek, V. Kolivoška and M. Hromadová, Tuning the Contact Conductance of Anchoring Groups in Single Molecule Junctions by Molecular Design, *Nanoscale*, 2019, **11**(27), 12959–12964.
24 M. Valášek and M. Mayor, Spatial and Lateral Control of Functionality by Rigid Molecular Platforms, *Chem. –Eur. J.*, 2017, **23**(55), 13538–13548.
25 Y. Yao and J. M. Tour, Facile Convergent Route to Molecular Caltrops, *J. Org. Chem.*, 1999, **64**(6), 1968–1971.
26 L. Zhu, Y. Harima, K. Yamashita, H. Tang, D. Hirayama, Y. Aso and T. Otsubo, Electrochemical Properties of Self-Assembled Monolayers of Tripod-Shaped Molecules and Their Applications to Organic Light-Emitting Diodes, *Chem. Commun.*, 2001, **18**, 1830–1831.
27 D. Hirayama, K. Takimiya, Y. Aso, T. Otsubo, T. Hasobe, H. Yamada, H. Imahori, S. Fukuzumi and Y. Sakata, Large Photocurrent Generation of Gold Electrodes Modified with [60]Fullerene-Linked Oligothiophenes Bearing a Tripodal Rigid Anchor, *J. Am. Chem. Soc.*, 2002, **124**(4), 532–533.
28 L. Wei, K. Padmaja, W. J. Youngblood, A. B. Lysenko, J. S. Lindsey and D. F. Bocian, Diverse Redox-Active Molecules Bearing Identical Thiol-Terminated Tripodal Tethers for Studies of Molecular Information Storage, *J. Org. Chem.*, 2004, **69**(5), 1461–1469.
29 L. Wei, H. Tiznado, G. Liu, K. Padmaja, J. S. Lindsey, F. Zaera and D. F. Bocian, Adsorption Characteristics of Tripodal Thiol-Functionalized Porphyrins on Gold, *J. Phys. Chem. B*, 2005, **109**(50), 23963–23971.
30 Y. Ie, T. Hirose, A. Yao, T. Yamada, N. Takagi, M. Kawai and Y. Aso, Synthesis of Tripodal Anchor Units Bearing Selenium Functional Groups and Their Adsorption Behaviour on Gold, *Phys. Chem. Chem. Phys.*, 2009, **11**(25), 4949–4951.
31 M. Lindner, M. Valášek, J. Homberg, K. Edelmann, L. Gerhard, W. Wulfhekel, O. Fuhr, T. Wächter, M. Zharnikov, V. Kolivoška, L. Pospíšil, G. Mészáros, M. Hromadová and M. Mayor, Importance of the Anchor Group Position (Para versus Meta) in Tetraphenylmethane

Tripods: Synthesis and Self-Assembly Features, *Chem. –Eur. J.*, 2016, **22**, 13218–13235.

32 M. Valášek, M. Lindner and M. Mayor, Rigid Multipodal Platforms for Metal Surfaces, *Beilstein J. Nanotechnol.*, 2016, **7**(1), 374–405.

33 T. Sebechlebská, J. Šebera, V. Kolivoška, M. Lindner, J. Gasior, G. Mészáros, M. Valášek, M. Mayor and M. Hromadová, Investigation of the Geometrical Arrangement and Single Molecule Charge Transport in Self-Assembled Monolayers of Molecular Towers Based on Tetraphenylmethane Tripod, *Electrochim. Acta*, 2017, **258**, 1191–1200.

34 V. Kolivoška, J. Šebera, T. Sebechlebská, M. Lindner, J. Gasior, G. Mészáros, M. Mayor, M. Valášek and M. Hromadová, Probabilistic Mapping of Single Molecule Junction Configurations as a Tool to Achieve the Desired Geometry of Asymmetric Tripodal Molecules, *Chem. Commun.*, 2019, **55**(23), 3351–3354.

35 F. J. Uribe-Romo, J. R. Hunt, H. Furukawa, C. Klöck, M. O'Keeffe and O. M. Yaghi, A Crystalline Imine-Linked 3-D Porous Covalent Organic Framework, *J. Am. Chem. Soc.*, 2009, **131**(13), 4570–4571.

36 J. K. Zaręba, Tetraphenylmethane and Tetraphenylsilane as Building Units of Coordination Polymers and Supramolecular Networks – A Focus on Tetraphosphonates, *Inorg. Chem. Commun.*, 2017, **86**, 172–186.

37 X. Guan, F. Chen, Q. Fang and S. Qiu, Design and Applications of Three Dimensional Covalent Organic Frameworks, *Chem. Soc. Rev.*, 2020, **49**(5), 1357–1384.

38 H. M. El-Kaderi, J. R. Hunt, J. L. Mendoza-Cortés, A. P. Côté, R. E. Taylor, M. O'Keeffe and O. M. Yaghi, Designed Synthesis of 3D Covalent Organic Frameworks, *Science*, 2007, **316**(5822), 268–272.

39 S. Wang, L. Da, J. Hao, J. Li, M. Wang, Y. Huang, Z. Li, Z. Liu and D. Cao, A Fully Conjugated 3D Covalent Organic Framework Exhibiting Band-like Transport with Ultrahigh Electron Mobility, *Angew. Chem., Int. Ed.*, 2021, **60**(17), 9321–9325.

40 J. Šebera, V. Kolivoška, M. Valášek, J. Gasior, R. Sokolová, G. Mészáros, W. Hong, M. Mayor and M. Hromadová, Tuning Charge Transport Properties of Asymmetric Molecular Junctions, *J. Phys. Chem. C*, 2017, **121**(23), 12885–12894.

41 M. A. Karimi, S. G. Bahoosh, M. Valášek, M. Bürkle, M. Mayor, F. Pauly, E. Scheer, N. Agraït, J. C. Cuevas and K. V. Mikkelsen, Identification of the Current Path for a Conductive Molecular Wire on a Tripodal Platform, *Nanoscale*, 2016, **8**(20), 10582–10590.

42 L. Gerhard, K. Edelmann, J. Homberg, M. Valášek, S. G. Bahoosh, M. Lukas, F. Pauly, M. Mayor and W. Wulfhekel, An Electrically Actuated Molecular Toggle Switch, *Nat. Commun.*, 2017, **8**, 14672.

43 M. Wu, Z. Shan, J. Wang, Z. Gu, X. Wu, B. Xu and G. Zhang, Three-Dimensional Covalent Organic Frameworks Based on a π-Conjugated Tetrahedral Node, *Chem. Commun.*, 2021, **57**(80), 10379–10382.

44 J. G. Park, M. L. Aubrey, J. Oktawiec, K. Chakarawet, L. E. Darago, F. Grandjean, G. J. Long and J. R. Long, Charge Delocalization and Bulk Electronic Conductivity in the Mixed-Valence Metal–Organic Framework Fe(1,2,3-Triazolate)$_2$(BF$_4$)$_x$, *J. Am. Chem. Soc.*, 2018, **140**(27), 8526–8534.

45 G. Chen, L. B. Gee, W. Xu, Y. Zhu, J. S. Lezama-Pacheco, Z. Huang, Z. Li, J. T. Babicz, S. Choudhury, T.-H. Chang, E. Reed, E. I. Solomon and Z. Bao, Valence-Dependent Electrical Conductivity in a 3D Tetrahydroxyquinone-Based Metal–Organic Framework, *J. Am. Chem. Soc.*, 2020, **142**(51), 21243–21248.

46 S. U. Koschmieder and G. Wilkinson, Homoleptic and Related Aryls of Transition Metals, *Polyhedron*, 1991, **10**(2), 135–173.

47 Y. Tanaka, Organometallics in Molecular Junctions: Conductance, Functions, and Reactions, *Dalton Trans.*, 2024, **53**(20), 8512–8523.

48 S. Rigaut, Metal Complexes in Molecular Junctions, *Dalton Trans.*, 2013, **42**(45), 15859.

49 A. Vezzoli, Metal Complexes and Clusters in Single-Molecule Electronics, in *Encyclopedia of Inorganic and Bioinorganic Chemistry*, Scott, R. A., Ed., Wiley, 2021, pp. 1–21.

50 M. Camarasa-Gomez, D. Hernangomez-Perez, M. Inkpen, G. Lovat, E.-D. Fung, X. Roy, L. Venkataraman and F. Evers, Mechanically-Tunable Quantum Interference in Ferrocene-Based Single-Molecule Junctions, *Nano Lett.*, 2020, **20**(9), 6381–6386.

51 H. E. Skipper, C. V. May, A. L. Rheingold, L. H. Doerrer and M. Kamenetska, Hard–Soft Chemistry Design Principles for Predictive Assembly of Single Molecule-Metal Junctions, *J. Am. Chem. Soc.*, 2021, **143**(40), 16439–16447.

52 C. Olivar, J. M. Parr, C. Avedian, T. Saal, L. Zagami, R. Haiges, M. Sharma and M. S. Inkpen, Osmium(IV) Tetraaryl Complexes Formed from Prefunctionalized Ligands, *Inorg. Chem.*, 2025, **64**(12), 6192–6204.

53 L. Zagami, T. Saal, C. Avedian and M. S. Inkpen, Intervalence Charge Transfer in an Osmium(IV) Tetra(Ferrocenylaryl) Complex, *Inorg. Chem.*, 2025, **64**(5), 2312–2320.

54 J. M. Parr, C. Olivar, T. Saal, R. Haiges and M. S. Inkpen, Pushing Steric Limits in Osmium(IV) Tetraaryl Complexes, *Dalton Trans.*, 2022, **51**, 10558–10570.

55 J. Arnold, G. Wilkinson, B. Hussain and M. B. Hursthouse, Redox Chemistry of the Homoleptic Aryl Os(2-MeC$_6$H$_4$)$_4$: Synthesis and Characterization of the First Osmium(v) Organometallic [Os(2-MeC$_6$H$_4$)$_4$][CF$_3$SO$_3$], *J. Chem. Soc. Chem. Commun.*, 1988, **20**, 1349–1350.

56 J. Arnold, G. Wilkinson, B. Hussain and M. B. Hursthouse, Reactivity of the Homoleptic Osmium Aryl Os(2-MeC$_6$H$_4$)$_4$: Ligand-Induced Reductive Coupling, .Sigma.- to .Pi.-Rearrangement, and Ortho-Hydrogen Activation, *Organometallics*, 1989, **8**(5), 1362–1369.

57 M.-K. Lau, Q.-F. Zhang, J. L. C. Chim, W.-T. Wong and W.-H. Leung, Direct Functionalisation of σ-Aryl Ligands: Preparation of Homoleptic Functionalised Aryls of Osmium(Iv), *Chem. Commun.*, 2001, **79**(16), 1478–1479.

58 R. P. Tooze, P. Stavropoulos, M. Motevalli, M. B. Hursthouse and G. Wilkinson, Synthesis and X-Ray Crystal Structures of the First Tetrahedral Osmium(IV) Compounds, Tetrakis(Cyclohexyl)Osmium(IV) and Tetrakis(o-Methylphenyl)Osmium(IV), *J. Chem. Soc. Chem. Commun.*, 1985, **16**, 1139.

59 H. B. Gray, Molecular Orbital Theory for Transition Metal Complexes, *J. Chem. Educ.*, 1964, **41**(1), 2.

60 R. S. Klausen, J. R. Widawsky, T. A. Su, H. Li, Q. Chen, M. L. Steigerwald, L. Venkataraman and C. Nuckolls, Evaluating Atomic Components in Fluorene Wires, *Chem. Sci.*, 2014, **5**(4), 1561–1564.

61 J. M. Brisendine, S. Refaely-Abramson, Z.-F. Liu, J. Cui, F. Ng, J. B. Neaton, R. L. Koder and L. Venkataraman, Probing Charge Transport through Peptide Bonds, *J. Phys. Chem. Lett.*, 2018, **9**(4), 763–767.

62 R. S. Klausen, J. R. Widawsky, M. L. Steigerwald, L. Venkataraman and C. Nuckolls, Conductive Molecular Silicon, *J. Am. Chem. Soc.*, 2012, **134**(10), 4541–4544.

63 T. A. Su, H. Li, R. S. Klausen, J. R. Widawsky, A. Batra, M. L. Steigerwald, L. Venkataraman and C. Nuckolls, Tuning Conductance in π–σ–π Single-Molecule Wires, *J. Am. Chem. Soc.*, 2016, **138**, 7791–7795.

64 J. Yang, W. He, K. Denman, Y. B. Jiang and Y. Qin, A Molecular Breakwater-like Tetrapod for Organic Solar Cells, *J. Mater. Chem. A*, 2015, **3**(5), 2108–2119.

65 E. A. Doud, M. S. Inkpen, G. Lovat, E. Montes, D. W. Paley, M. L. Steigerwald, H. Vázquez, L. Venkataraman and X. Roy, In Situ Formation of N-Heterocyclic Carbene-Bound Single-Molecule Junctions, *J. Am. Chem. Soc.*, 2018, **140**(28), 8944–8949.

66 J. Arnold, G. Wilkinson, B. Hussain and M. B. Hursthouse, Synthesis and X-Ray Crystal Structure of Tetra(2-Methylphenyl)Molybdenum(IV), $Mo(2\text{-}MeC_6H_4)_4$. Redox Chemistry of $M(2\text{-}MeC_6H_4)_4$ Compounds of Molybdenum, Rhenium, Ruthenium, and Osmium, *Dalton Trans.*, 1989, **11**, 2149.

67 M.-K. Lau, J. L. Chim, W.-T. Wong, I. D. Williams and W.-H. Leung, Synthesis and Molecular Structures of Monooxo Aryl Complexes of Osmium(VI), *Can. J. Chem.*, 2001, **79**(5–6), 607–612.

68 D. T. Hardy, G. Wilkinson and G. B. Young, Mechanistic Studies of Ligand-Induced Thermolytic Reductive Elimination of Biaryl from Tetraarylosmium(IV), *Polyhedron*, 1996, **15**(8), 1363–1373.

69 E. Larsen and G. N. La Mar, The Angular Overlap Model. How to Use It and Why, *J. Chem. Educ.*, 1974, **51**(10), 633.

70 L. Venkataraman, J. E. Klare, I. W. Tam, C. Nuckolls, M. S. Hybertsen and M. L. Steigerwald, Single-Molecule Circuits with Well-Defined Molecular Conductance, *Nano Lett.*, 2006, **6**(3), 458–462.

71 A. I. Yanson, G. Rubio Bollinger, H. E. Van Den Brom, N. Agraït and J. M. Van Ruitenbeek, Formation and Manipulation of a Metallic Wire of Single Gold Atoms, *Nature*, 1998, **395**(6704), 783–785.

72 S. Y. Quek, M. Kamenetska, M. L. Steigerwald, H. J. Choi, S. G. Louie, M. S. Hybertsen, J. B. Neaton and L. Venkataraman, Mechanically Controlled Binary Conductance Switching of a Single-Molecule Junction, *Nat. Nanotechnol.*, 2009, **4**(4), 230–234.

73 P. Stavropoulos, P. D. Savage, R. P. Tooze, G. Wilkinson, B. Hussain, M. Motevalli and M. B. Hursthouse, The Synthesis and X-Ray Crystal Structures of Homoleptic Tetrahedral Aryls of Osmium(IV) and of Cyclohexyls of Ruthenium(IV), Osmium(IV), and Chromium(IV), *Dalton Trans.*, 1987, **3**, 557.

74 S. Y. Quek, H. J. Choi, S. G. Louie and J. B. Neaton, Length Dependence of Conductance in Aromatic Single-Molecule Junctions, *Nano Lett.*, 2009, **9**(11), 3949–3953.

75 P. Makk, D. Tomaszewski, J. Martinek, Z. Balogh, S. Csonka, M. Wawrzyniak, M. Frei, L. Venkataraman and A. Halbritter, Correlation Analysis of Atomic and Single-Molecule Junction Conductance, *ACS Nano*, 2012, **6**(4), 3411–3423.

76 V. Fatemi, M. Kamenetska, J. B. Neaton and L. Venkataraman, Environmental Control of Single-Molecule Junction Transport, *Nano Lett.*, 2011, **11**(5), 1988–1992.

77 S. Kawai, Discussion on Decomposition of Chloroform, *Yakugaku Zasshi*, 1966, **86**(12), 1125–1132.

78 O. Traverso and F. Scandola, Photooxidation of Ferrocene in Halocarbon Solvents, *Inorg. Chim. Acta.*, 1970, **4**, 493–498.

79 L. A. Nagahara, T. Thundat and S. M. Lindsay, Preparation and Characterization of STM Tips for Electrochemical Studies, *Rev. Sci. Instrum.*, 1989, **60**(10), 3128–3130.

80 B. Capozzi, J. Z. Low, J. Xia, Z.-F. Liu, J. B. Neaton, L. M. Campos and L. Venkataraman, Mapping the Transmission Functions of Single-Molecule Junctions, *Nano Lett.*, 2016, **16**(6), 3949–3954.

81 J. Z. Low, B. Capozzi, J. Cui, S. Wei, L. Venkataraman and L. M. Campos, Tuning the Polarity of Charge Carriers Using Electron Deficient Thiophenes, *Chem. Sci.*, 2017, **8**(4), 3254–3259.

82 B. Capozzi, J. Xia, O. Adak, E. J. Dell, Z.-F. Liu, J. C. Taylor, J. B. Neaton, L. M. Campos and L. Venkataraman, Single-Molecule Diodes with High Rectification Ratios through Environmental Control, *Nat. Nanotechnol.*, 2015, **10**(6), 522–527.

83 V. Blum, R. Gehrke, F. Hanke, P. Havu, V. Havu, X. Ren, K. Reuter and M. Scheffler, Ab Initio Molecular Simulations with Numeric Atom-Centered Orbitals, *Comput. Phys. Commun.*, 2009, **180**(11), 2175–2196.

84 M. Camarasa-Gómez, D. Hernangómez-Pérez, J. Wilhelm, A. Bagrets and F. Evers, Molecular Transport, *arXiv*, 2024, preprint, arXiv:2411.01680, DOI: 10.48550/arXiv.2411.01680.

85 M. Camarasa-Gómez, D. Hernangómez-Pérez and F. Evers, Spin–Orbit Torque in Single-Molecule Junctions from Ab Initio, *J. Phys. Chem. Lett.*, 2024, **15**(21), 5747–5753.

86 A. Arnold, F. Weigend and F. Evers, Quantum Chemistry Calculations for Molecules Coupled to Reservoirs: Formalism, Implementation, and Application to Benzenedithiol, *J. Chem. Phys.*, 2007, **126**(17), 174101.

87 A. Bagrets, Spin-Polarized Electron Transport Across Metal–Organic Molecules: A Density Functional Theory Approach, *J. Chem. Theory Comput.*, 2013, **9**(6), 2801–2815.

88 J. P. Perdew, K. Burke and M. Ernzerhof, Generalized Gradient Approximation Made Simple, *Phys. Rev. Lett.*, 1996, **77**(18), 3865–3868.
89 F. Evers, R. Korytár, S. Tewari and J. M. Van Ruitenbeek, Advances and Challenges in Single-Molecule Electron Transport, *Rev. Mod. Phys.*, 2020, **92**(3), 35001.
90 M. Thoss and F. Evers, Perspective: Theory of Quantum Transport in Molecular Junctions, *J. Chem. Phys.*, 2018, **148**(3), 30901.
91 C. R. Prindle, W. Shi, L. Li, J. D. Jensen, B. W. Laursen, M. L. Steigerwald, C. Nuckolls and L. Venkataraman, Effective Gating in Single-Molecule Junctions through Fano Resonances, *J. Am. Chem. Soc.*, 2024, **146**, 3646–3650.
92 C. J. Lambert, W. Osikowicz, Y. Wang, W. R. Salaneck, A. Mishchenko, T. Wandlowski, M. Mayor, G. Schoen, F. Pauly, J. B. Neaton, J. E. Macdonald and R. J. Nichols, Basic Concepts of Quantum Interference and Electron Transport in Single-Molecule Electronics, *Chem. Soc. Rev.*, 2015, **44**(4), 875–888.
93 L. Venkataraman, Y. S. Park, A. C. Whalley, C. Nuckolls, M. S. Hybertsen and M. L. Steigerwald, Electronics and Chemistry: Varying Single-Molecule Junction Conductance Using Chemical Substituents, *Nano Lett.*, 2007, **7**(2), 502–506.
94 J. Paier, M. Marsman and G. Kresse, Why Does the B3LYP Hybrid Functional Fail for Metals?, *J. Chem. Phys.*, 2007, **127**(2), 024103.
95 P. G. Edwards, T. Behling, G. Wilkinson, M. Motevalli and M. B. Hursthouse, Oxoaryls of Rhenium-(V) and -(VI) and Osmium(VI). X-Ray Crystal Structures of Dimesityldioxorhenium(VI), Tetramesityloxorhenium(VI), and Dimesityldioxoosmium(VI), *J. Chem. Soc. Dalton Trans.*, 1987, 169–175.
96 E. Epifanovsky, A. T. B. Gilbert, X. Feng, J. Lee, Y. Mao, N. Mardirossian, P. Pokhilko, A. F. White, M. P. Coons, A. L. Dempwolff, Z. Gan, D. Hait, P. R. Horn, L. D. Jacobson, I. Kaliman, J. Kussmann, A. W. Lange, K. U. Lao, D. S. Levine, J. Liu, S. C. McKenzie, A. F. Morrison, K. D. Nanda, F. Plasser, D. R. Rehn, M. L. Vidal, Z. Q. You, Y. Zhu, B. Alam, B. J. Albrecht, A. Aldossary, E. Alguire, J. H. Andersen, V. Athavale, D. Barton, K. Begam, A. Behn, N. Bellonzi, Y. A. Bernard, E. J. Berquist, H. G. A. Burton, A. Carreras, K. Carter-Fenk, R. Chakraborty, A. D. Chien, K. D. Closser, V. Cofer-Shabica, S. Dasgupta, M. De Wergifosse, J. Deng, M. Diedenhofen, H. Do, S. Ehlert, P. T. Fang, S. Fatehi, Q. Feng, T. Friedhoff, J. Gayvert, Q. Ge, G. Gidofalvi, M. Goldey, J. Gomes, C. E. González-Espinoza, S. Gulania, A. O. Gunina, M. W. D. Hanson-Heine, P. H. P. Harbach, A. Hauser, M. F. Herbst, M. Hernández Vera, M. Hodecker, Z. C. Holden, S. Houck, X. Huang, K. Hui, B. C. Huynh, M. Ivanov, Á. Jász, H. Ji, H. Jiang, B. Kaduk, S. Kähler, K. Khistyaev, J. Kim, G. Kis, P. Klunzinger, Z. Koczor-Benda, J. H. Koh, D. Kosenkov, L. Koulias, T. Kowalczyk, C. M. Krauter, K. Kue, A. Kunitsa, T. Kus, I. Ladjánszki, A. Landau, K. V. Lawler, D. Lefrancois, S. Lehtola, R. R. Li, Y. P. Li, J. Liang, M. Liebenthal, H. H. Lin, Y. S. Lin, F. Liu, K. Y. Liu, M. Loipersberger, A. Luenser, A. Manjanath, P. Manohar, E. Mansoor, S. F. Manzer, S. P. Mao, A. V. Marenich, T. Markovich, S. Mason, S. A. Maurer, P. F. McLaughlin, M. F. S. J. Menger, J. M. Mewes, S. A. Mewes, P. Morgante, J. W. Mullinax, K. J. Oosterbaan, G. Paran, A. C. Paul, S. K. Paul, F. Pavošević, Z. Pei, S. Prager, E. I. Proynov, Á. Rák, E. Ramos-Cordoba, B. Rana, A. E. Rask, A. Rettig, R. M. Richard, F. Rob, E. Rossomme, T. Scheele, M. Scheurer, M. Schneider, N. Sergueev, S. M. Sharada, W. Skomorowski, D. W. Small, C. J. Stein, Y. C. Su, E. J. Sundstrom, Z. Tao, J. Thirman, G. J. Tornai, T. Tsuchimochi, N. M. Tubman, S. P. Veccham, O. Vydrov, J. Wenzel, J. Witte, A. Yamada, K. Yao, S. Yeganeh, S. R. Yost, A. Zech, I. Y. Zhang, X. Zhang, Y. Zhang, D. Zuev, A. Aspuru-Guzik, A. T. Bell, N. A. Besley, K. B. Bravaya, B. R. Brooks, D. Casanova, J. D. Chai, S. Coriani, C. J. Cramer, G. Cserey, A. E. Deprince, R. A. Distasio, A. Dreuw, B. D. Dunietz, T. R. Furlani, W. A. Goddard, S. Hammes-Schiffer, T. Head-Gordon, W. J. Hehre, C. P. Hsu, T. C. Jagau, Y. Jung, A. Klamt, J. Kong, D. S. Lambrecht, W. Liang, N. J. Mayhall, C. W. McCurdy, J. B. Neaton, C. Ochsenfeld, J. A. Parkhill, R. Peverati, V. A. Rassolov, Y. Shao, L. V. Slipchenko, T. Stauch, R. P. Steele, J. E. Subotnik, A. J. W. Thom, A. Tkatchenko, D. G. Truhlar, T. Van Voorhis, T. A. Wesolowski, K. B. Whaley, H. L. Woodcock, P. M. Zimmerman, S. Faraji, P. M. W. Gill, M. Head-Gordon, J. M. Herbert and A. I. Krylov, Software for the Frontiers of Quantum Chemistry: An Overview of Developments in the Q-Chem 5 Package, *J. Chem. Phys.*, 2021, **155**, 084801, DOI: 10.1063/5.0055522.
97 E. V. Lenthe, E. J. Baerends and J. G. Snijders, Relativistic Regular Two-Component Hamiltonians, *J. Chem. Phys.*, 1993, **99**(6), 4597–4610.
98 CCDC 2480811: Experimental Crystal Structure Determination, 2026, DOI: 10.5517/ccdc.csd.cc2p8h5n.